Journal of Materials Chemistry A

PAPER

View Article Online
View Journal | View Issue

Cite this: J. Mater. Chem. A, 2018, 6, 12682

Photocatalytic and electrically conductive transparent Cl-doped ZnO thin films *via* aerosol-assisted chemical vapour deposition†

Arreerat Jiamprasertboon,[ab] Michael J. Powell,[b] Sebastian C. Dixon,[b] Raul Quesada-Cabrera,[b] Abdullah M. Alotaibi,[b] Yao Lu,[c] Aoyun Zhuang,[b] Sanjayan Sathasivam,[b] Theeranun Siritanon,[a] Ivan P. Parkin[b] and Claire J. Carmalt[*b]

A simple, economical and effective solution-based chemical vapour deposition (CVD) technique, aerosol-assisted CVD, has been successfully applied to produce inexpensive Cl-doped ZnO films using Zn acetate dihydrate and $FeCl_3$. X-ray photoelectron spectroscopy and the increase in cell parameters from powder X-ray diffraction determined that Cl had been doped into the wurtzite ZnO lattice. The Cl-doping had a significant effect on the morphology of the thin films synthesised and resulted in an improvement in the visible light transmission and lower electrical resistance (typical resistivities of doped films $\sim 10^{-2}$ Ω cm). The highest transmittance (% *T*) of 85% was obtained when 7 mol% $FeCl_3$ was used in the precursor solution and the lowest resistivity of $4.28 \pm 0.41 \times 10^{-2}$ Ω cm was obtained with 5 mol% $FeCl_3$. The greatest photocatalytic activity of stearic acid degradation under UVA irradiation was obtained on using 10 mol% $FeCl_3$, resulting in the highest formal quantum efficiency (FQE) of $3.0 \pm 0.1 \times 10^{-4}$ molecule per photon. These films, therefore, display transparent conducting oxide and photocatalytic properties, giving multifunctional characteristics and promising applications.

Received 9th February 2018
Accepted 11th June 2018

DOI: 10.1039/c8ta01420e

rsc.li/materials-a

Introduction

Transparent conducting oxide (TCO) materials have the unique coexistent properties of high optical transparency and high electrical conductivity that contribute to various electronic devices such as liquid crystal displays (LCDs), touch panel screens, E-paper, defrosting windows, electrochromic windows and mirrors, photovoltaics, flexible electronics and invisible security circuits.[1,2] Semiconducting oxides with large band gap energies (>3.1 eV) and the ability to be doped to generate low resistivity ($<10^{-2}$ Ω cm) are required for TCO properties.[3] Even though Sn-doped In_2O_3 (ITO) and F-doped SnO_2 (FTO) are the most widely used TCOs because of their excellent properties of low electrical resistivity with high transparency,[1,4–6] In_2O_3 has the disadvantages of high cost of extraction and processing, as well as concern over the relative scarcity of indium ores. Sn also has also suffers from price fluctuations compared to other elements, such as Zn.[7]

Zinc oxide (ZnO) is a promising candidate for TCOs because it is well known as an intrinsic n-type semiconductor with a wide band gap of *ca.* 3.37 eV; moreover, it has high thermal stability,[8] is inexpensive, earth abundant and relatively nontoxic compared to ITO and FTO.[8–12] Doping is a strategy to enhance the electrical conductivity of TCO materials. Cation dopants such as Al^{3+}, Ga^{3+}, In^{3+},[13–19] Sc^{3+},[20] Si^{4+} (ref. 21 and 22) and Cu^{23} and anion dopants such as F^-,[16,24,25] Cl^- (ref. 26) and N^{3-},[27] have all been successfully incorporated into ZnO thin films. Anion doping is considered to be a superior route to obtain high carrier concentration and mobility while maintaining high transparency, because the conduction band (CB) is less perturbed by the dopant and thus the scattering of electrons in the CB is minimized.[1] F-Doping has been extensively studied and the resulting materials show excellent properties,[5,28,29] investigations on the use of other anions, such as Cl, are relatively limited. However, there have been some reports on the electrical, optical and photoelectrochemical properties of Cl-doped ZnO, which show the potential of Cl doping.[30–35] Therefore, we were interested in exploring further the novel properties of ZnO:Cl, in particular the film deposition method which has been shown to play a key role in modifying the film properties. Aerosol-assisted chemical vapour deposition (AACVD) is an effective technique to control the morphology and

[a]School of Chemistry, Institute of Science, Suranaree University of Technology, 111 University Avenue, Muang, Nakhon Ratchasima, 30000, Thailand. E-mail: c.j.carmalt@ucl.ac.uk

[b]Material Chemistry Centre, Department of Chemistry, University College London, 20 Gordon Street, London, WC1H 0AJ, UK

[c]Department of Mechanical Engineering, University College London, London, WC1E 7JE, UK

† Electronic supplementary information (ESI) available. See DOI: 10.1039/c8ta01420e

simultaneously the properties of the deposited films.[36] Moreover, it is a simple, sustainable and scalable deposition film fabrication technique[37] that allows for the use of a variety of precursors with appropriate solubility in a suitable solvent.[12] In the procedure, soluble halide precursors can be utilised which are generally cheaper than metal–organic precursors.[38]

In general, TCO films have poor photocatalytic activity and photocatalytic films show poor TCO properties.[39] For example, W-doped TiO_2 and Nb-doped TiO_2 films are good photocatalysts and electrically conductive (resistivities were 6.3×10^{-1} to 6.3×10^{-2} Ω cm and 5.8×10^{-2} to 1.3×10^{-3} Ω cm, respectively) but they are coloured;[40,41] P-doped TiO_2 films are also good photocatalysts but their conductivity (resistivities were 1.69–6.49 Ω cm) as well as transparency (% T is less than 80%) have not yet passed the requirement to be considered good TCO materials.[42] In general, multifunctional properties are not commonly observed in most films. The ability to synthesize films that display both good electrical and photocatalytic properties whilst being transmissive of visible wavelengths would therefore be of benefit for multifunctional devices.

Here, the Cl-doped ZnO films were prepared by a simple, economical and potential film deposition, AACVD technique for the first time. Photocatalytic properties of ZnO:Cl films are first observed. Photocatalytic transparent conducting Cl-doped ZnO thin films are described as promising materials for sustainable applications.

Experimental

Film synthesis

All films were synthesised *via* aerosol assisted chemical vapor deposition (AACVD). Zn(II) acetate dihydrate, $Zn(OAc)_2 \cdot 2H_2O$, (≥98%, Sigma-Aldrich) and ferric chloride anhydrous, $FeCl_3$, (98%, Aldrich) were used as the Zn and Cl precursors respectively. All precursors were used as received without further purification. Methanol (99.9%, Fisher Scientific) was used as the solvent. Nitrogen gas (99.99%, BOC) was used as the carrier gas.

In a typical deposition, the precursor solution was prepared by dissolving $Zn(OAc)_2 \cdot 2H_2O$ (0.50 g, 2.28 mmol) in methanol (20 mL). $FeCl_3$ was dissolved in methanol and then added to the zinc acetate solution in the corresponding mol% of 0, 1, 3, 5, 7, 10 and 15. Each precursor was stirred until separately for *ca.* 5 minutes and then mixed by stirring to give the final precursor solution. A glass substrate, coated with a 50 nm SiO_2 barrier layer (NSG Pilkington Ltd), with the dimension of 3.2 mm × 45 mm × 100 mm was used. The SiO_2 barrier layer is important to prevent leeching of ions between the substrate and the film. Prior to depositing, the substrate was cleaned by detergent, isopropanol and acetone, respectively. The AACVD apparatus is illustrated in Fig. 1. The substrate was placed on a carbon heating block, which was enclosed in a quartz tube. The top plate of stainless steel of 4.8 cm × 15 cm was suspended over the substrate approximately 8 mm to assist the laminar flow of the aerosol. In the deposition, the obtained precursor solution was atomised using a 'Liquifog' piezo ultrasonic humidifiers (Johnson Matthey). The aerosol or mist was generated and transported to the heated substrate through the baffle *via* nitrogen carrier gas with a flow rate of 1.5 L min^{-1}. The deposition temperature was 500 °C for all samples. A typical deposition would take 15–20 minutes in order for all of the solution to aerosolize, after which the substrate was left to cool under a continuous flow of nitrogen gas and removed when the temperature of reactor was below 100 °C. The film was cut into pieces of 1 × 1 cm^2 prior to the characterisations.

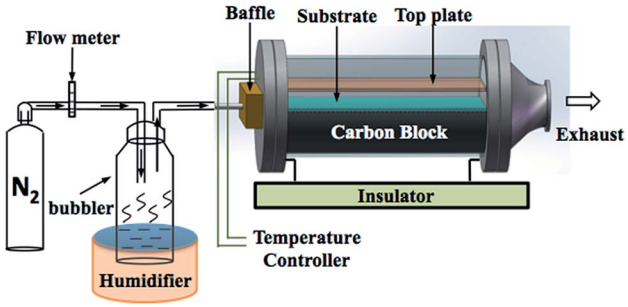

Fig. 1 The schematic illustration of aerosol assisted chemical vapour deposition (AACVD) apparatus.

Film characterisation

X-ray photoelectron spectroscopy (XPS) spectra of Zn 2p, Fe 2p, Cl 2p and O 1s were investigated to confirm the oxidation states as well as compositions of constituent elements. A Thermo Scientific K-alpha spectrometer with a monochromatic Al Kα radiation, a dual beam charge compensation system and constant pass energy of 50 eV were utilised. The collected spectra were fitted using CasaXPS software. The C 1s peaks at 284.5 eV were used as reference for binding energy calibration. X-ray diffraction (XRD) measurement, using a Bruker-Axs D8 X-ray diffractometer with parallel beam optics equipped with a PSD LynxEye silicon strip detector, was performed to check the phase purity of the films. Monochromatic Cu $K_{\alpha 1}$ and $K_{\alpha 2}$ X-rays (λ = 1.54056 Å and 1.54439 Å, respectively), with the intensity ratio of 2 : 1, were generated using a voltage of 40 kV and a current of 40 mA. The incident beam angle was kept at a grazing setup of 1°. XRD patterns were collected with 2θ range of 10–66° with a step size of 0.05° by a scan rate of 4 s per step. Le Bail refinement using GSAS and EXPGUI software[43,44] was done to get the cell parameters. Scanning electron microscope (SEM) images and side-on SEM images were gained to study the surface morphology and film thickness, respectively, using a JEOL JSM-6301F Field Emission instrument with an operated acceleration voltage of 10 kV. UV/vis transmittance spectra were measured to obtain the optical properties by using a Perkin Elmer Lambda 950 UV/vis/NIR Spectrophotometer. Surface topology and roughness (root mean squared, R_q) were characterised using an atomic force microscope (AFM, Bruker Multimode 8). The tips were used in the ScanAsyst tapping mode to scan the area of 1.0 μm × 1.0 μm, respectively, with 512 scans.

Hall effect measurement with the van der Pauw method was carried out on an Ecopia HMS-3000 to investigate the electrical properties: resistivity (ρ), carrier concentration (n) and carrier

mobility (μ). A magnetic field of 0.58 T and an input current of 1 μA to 1 mA were applied for the measurement.

To determine the photocatalytic properties, the test of stearic acid degradation was studied. A thin layer of stearic acid was coated on films by dipping in a 0.05 M stearic acid solution in chloroform using a bespoke dip coating apparatus, which withdraws the substrate at a fixed rate vertically from the stearic acid solution. Fourier transform infrared (FTIR) spectra were collected in the absorbance mode in the range of 2700–3000 cm^{-1}, using a Perkin Elmer RX-I instrument, to monitor the C–H bond decomposition under UVA (λ = 365 nm) light exposure. A 2 × 8 W blacklight-bulb (BLB) UVA lamps (Vilber-Lourmat) with the irradiation of ~0.5 mW cm^{-2}, as measured by a UVX meter (UVP), were used in the test. The linear regression of the initial 30–40% degradation steps (zero-order kinetics) with a conversion factor (1 $cm^{-1} \approx 9.7 \times 10^{15}$ molecule of stearic acid per cm^2)[45] was utilised to determine the photocatalytic activity rates as formal quantum efficiency (FQE) value.

Results and discussion

Film synthesis

In the synthesis, the precursors $Zn(OAc)_2 \cdot 2H_2O$ and $FeCl_3$ were dissolved in methanol. At low concentrations (below 5 mol%) of $FeCl_3$ the solution was clear and colourless. However, at higher concentrations (>5 mol% of $FeCl_3$) some white colloid was observed in the mixed solution, which may result due to the formation of iron hydroxides or iron oxohydroxochlorido species. The undoped ZnO films deposited were typically darker in hue than the doped films. This was attributed to higher carbon contamination in the undoped films, which was confirmed by the presence of C 1s XPS spectra in the bulk of films. The prepared films become more transparent with increasing the amount of $FeCl_3$. Fig. 2 shows a photograph of the most transparent films prepared using 7 mol% $FeCl_3$ in the solution precursor (right) compared with bare glass (left). The 15 mol% $FeCl_3$-loaded precursor solution resulted in the deposition of a hazy film and hence it was not further characterised for optical and electrical properties.

All the films had good adhesion to the substrate, passing the Scotch tape test and steel scalpel scratch test. The films showed good stability after six months storage under ambient condition and they were stable to common solvents such as methanol, isopropanol, acetone and chloroform. All films were deposited at 500 °C, since this temperature resulted in films with the optimum appearance, good coverage and the best electrical properties, in comparison to films deposited at 400 °C and 550 °C.

Fig. 2 Photograph of bare glass (left) and 7 mol% $FeCl_3$ loaded ZnO film (right).

Elemental analysis

The chemical components and their oxidation states were studied by X-ray photoelectron spectroscopy (XPS) which indicated that Cl-doped ZnO thin films had been deposited. XPS core level spectra for Zn 2p, Fe 2p, Cl 2p and O 1s were performed. No Fe was observed in any of the samples (both surface and depth profiling). It has been previously reported that Fe can substitute at the Zn site in ZnO films, which can be in the form of either Fe^{2+} [ref. 46–48] or Fe^{3+} [ref. 49–52] or mixed Fe^{2+}/Fe^{3+}.[53,54] However, no Fe substitution was observed in these films deposited *via* AACVD. This could be a result of side reactions occurring in the solution, such as a ligand exchange, yielding iron acetate. Indeed, after some AACVD depositions, a red precipitate was observed in the bubbler which may be iron acetate as this is insoluble and has been described previously as a red solid if impure or mixed iron/zinc acetates (ESI†).[55,56] Furthermore, this would result in Zn^{2+} and Cl^- being present in higher concentrations in the precursor solution. However, other reactions are also possible, for example anhydrous $FeCl_3$ undergoes hydrolysis to produce HCl and iron hydroxide and the presence of HCl could result in Cl-doping.

Zn 2p and O 1s spectra of all films show similar features; therefore the Cl-doped ZnO films formed using 10 mol% $FeCl_3$ has been chosen as a representative example and is shown in Fig. 3(a) and (b). The Zn $2p_{3/2}$ peak, observed at 1020.6 (±0.2) eV, was assigned to Zn^{2+}–O bond (Fig. 2a).[57,58] The O 1s spectrum (Fig. 3b) can be deconvoluted into two peaks; the peak at 529.5 (±0.2) eV, corresponds to O^{2-} in the lattice and the peak at 531.4 (±0.2) eV can be attributed to oxygen vacancies or loosely bound oxygen species, such as adsorbed O_2 and –OH. This oxygen is related to chemisorption on the surface and at the grain boundaries of the polycrystalline films.[59–62] The Cl 2p XPS spectra of all the Cl-doped films are shown in Fig. 3c, indicating that Cl was introduced into the films. The Cl $2p_{3/2}$ peak at around 198.4 (±0.2) eV corresponds to Cl–Zn bond. All XPS values quoted correspond to those observed in the literature.[30,32,33]

Although chlorine was detected within the XPS data, the signal was weak with a low signal to noise ratio, hence the at% of chlorine in all the Cl-doped samples was considered to be below 1 at%, as this is the threshold of reliable detection for XPS. Therefore, although chlorine can be detected and the influence of Cl can be seen in the change in preferential orientation and lattice parameters from the XRD data (*vide infra*), the measured values cannot be included as the error on these would be greater than the value calculated from the XPS data. Moreover, the calculated at% of Cl in the bulk by depth profile was lower than that at the surface and less than 1 at%

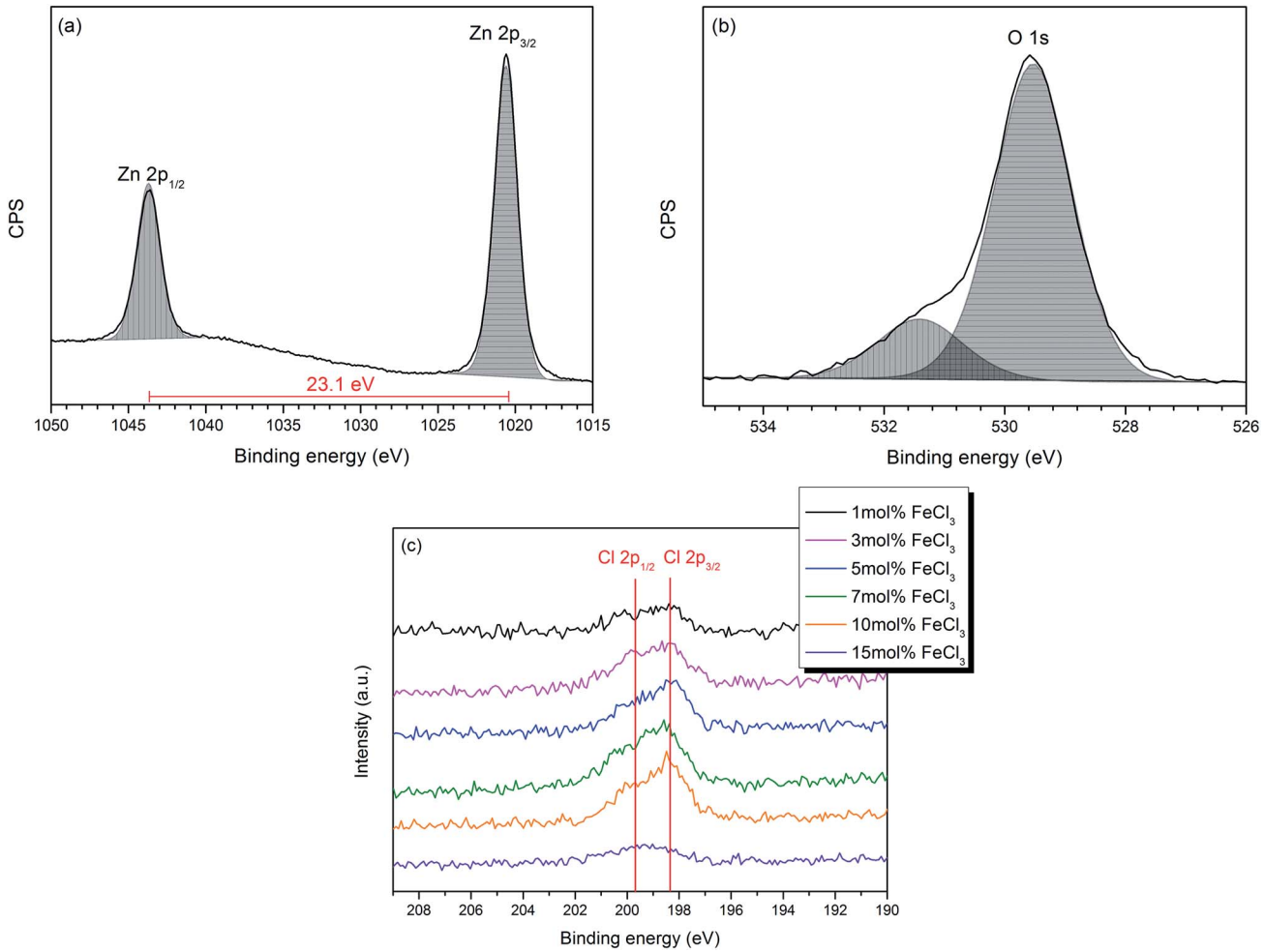

Fig. 3 High-resolution XPS spectra of (a) Zn $2p_{3/2}$ (b) O 1s of the Cl-doped ZnO film formed from 10 mol% $FeCl_3$ and (c) Cl 2p for all films.

(see ESI†). This suggests that the Cl concentration in the bulk was considerably lower due to preferential sputtering of Cl during the etching process, when Ar^+ ion bombardment was performed, as it is a light element similar to F,[16] O[63] and S.[64]

Crystal structure

XRD patterns of all films (Fig. 4) can be indexed as the single phase of hexagonal wurtzite ZnO (space group: $P6_3mc$). The preferred orientation illustrates itself through differences in peak intensity from sample to sample. This generally occurs during the film growth in order to minimise the internal stress and surface energy.[65] ZnO films have the preferred orientation of (002) plane along the *c*-axis which is normally observed in ZnO films as a result of film growth mechanism resulting in the most densely-packed and thermodynamically-favourable plane in the wurtzite structure.[66] The preferred orientation changed to the (101) plane for the Cl-doped ZnO films formed using 1–5 mol% $FeCl_3$ and then back to the (002) on increasing the amount of $FeCl_3$ (7–15 mol%). It is worth noting that the (101) plane preferred orientation was observed in the case of Cl-doped ZnO films prepared by atomic layer deposition[32] and Cl-doped ZnO nanospheres[67] and microdisks,[68] whereas the

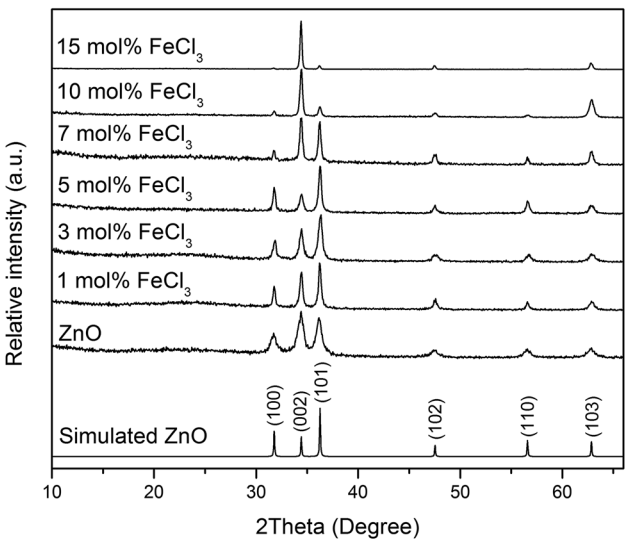

Fig. 4 XRD patterns of simulated bulk ZnO (ICSD #82028), undoped and Cl-doped ZnO thin films. All films can be indexed as the single phase of wurtzite ZnO.

(002) plane was observed for Cl-doped ZnO nanodisks[69] and nanowires.[70] This suggests that the preparation methods and form of sample influences the preferred orientation. Cell parameters *a*, *c* and cell volume (Fig. 5), which were obtained from Le Bail refinement, increased from undoped to Cl-doped ZnO films. This is expected for incorporation of Cl into the ZnO structure, since a comparison of ionic radii indicates that O^{2-} ($r_i = 1.40$ Å) is substituted by the bigger anion Cl^- ($r_i = 1.81$ Å).[71]

Surface morphology

SEM images (Fig. 6) illustrate that the morphology of the ZnO films can be affected by Cl doping. This can be rationalised from the preferred orientation change, which can be seen from XRD patterns (Fig. 4). The inclusion of Cl into the ZnO lattice had a significant effect on the surface morphology, such that even low levels of Cl in solution caused a change in the grain shape, as can be seen in the film formed using 5 mol% $FeCl_3$. It was also observed that the average grain size increased with the increase of mol% $FeCl_3$; this corresponds to the increase in crystallite size determined from Scherrer analysis (Table 1). The morphology present in the samples was different to Cl-doped ZnO films prepared *via* ALD, which was expected due to the effect of the different deposition techniques.[32] However, the morphology changed to hexagonal for the film formed using 15 mol% $FeCl_3$, this was also observed in ZnO thin films formed with acetic acid added to the precursor solution.[72] Side-on SEM images (Fig. 6, inset) were used to gain the thickness of the films, which are given in Table 1.

Surface topology

AFM images (Fig. 7) show the topology of the films and give information about the film roughness, which is reported as the root mean squared (rms) roughness value. The undoped ZnO film had a rms of 12.9 ± 2.2 nm while the Cl-doped ZnO formed from 10 mol% $FeCl_3$ had a similar rms of 15.4 ± 2.0 nm. Interestingly, the surface area difference of the undoped ZnO film and the Cl-doped ZnO formed from 10 mol% $FeCl_3$ were not significantly different.

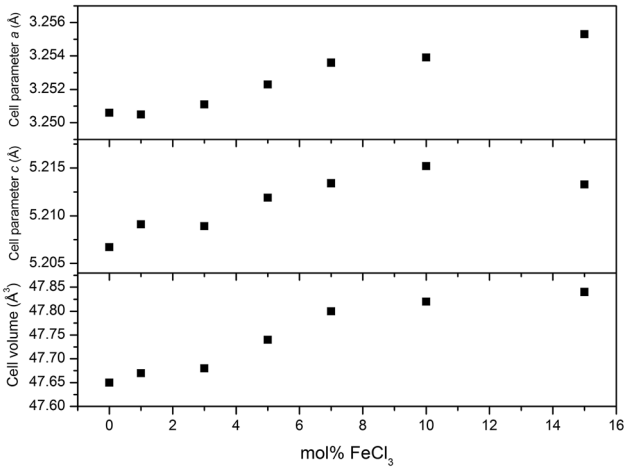

Fig. 5 Variation of cell parameters *a*, *c* and cell volume of the films with a change of mol% $FeCl_3$ added to the precursor solution. The increase of cell parameters confirms the incorporation of Cl into the ZnO lattice.

Functional properties

Photocatalytic properties. The photocatalytic properties of the films were investigated during degradation of stearic acid under UVA irradiation. The photocatalytic reaction can be described as:[73]

$$CH_3(CH_2)_{16}CO_2H + 26O_2 \xrightarrow{ZnO(h\nu \geq E_g)} 18CO_2 + 18H_2O \quad (1)$$

The results of the photocatalytic testing are conveniently expressed in terms of formal quantum efficiency (ξ), which indicates the number of stearic acid molecules degraded per incident photon. It can be seen in Fig. 8 that the activity of the pure ZnO film was extremely poor whilst addition of small amounts of Cl precursor had a dramatic effect on photocatalytic performance. The best activities were recorded for the film deposited from 10 mol% $FeCl_3$ with the highest ξ of $3.0 \pm 0.1 \times 10^{-4}$ molecule per photon, which was about 18 times greater than that of undoped ZnO film.

The improved photocatalytic efficiency of Cl doped ZnO thin films compared with undoped ZnO thin films were likely due to changes in morphology, as shown in the SEM images (Fig. 6). Morphology is reported to be one of the most important factors affecting the photocatalytic activity. The changes in morphology come from the defect point in crystalline structure after Cl incorporation into the ZnO lattice, this allows us to believe that more reactive centres are produced and therefore causes the enhanced photocatalytic process.[74] Moreover, crystal face exposition is also an important factor[75,76] since it was reported that the (101) plane show higher photocatalytically activity than that of (001) in ZnO.[77] This agrees with our work where (101) is the preferred orientation in some films. However, many factors need to be taken into consideration for the enhancement in photocatalytic efficiency, which cannot be concluded by a sole factor.

Transparent conducting oxide (TCO) properties

Optical properties. Fig. 9 shows the transmittance spectrum of all the films. The glass used as the substrate showed a % $T_{\lambda 400-700}$ of 89%. The undoped ZnO films displayed relatively low transmittance in the visible region, 68% (λ = 400–700 nm), as previously discussed this is attributed to carbon contamination. The Cl-doped ZnO films all displayed higher transparency; the films deposited using 5–10 mol% $FeCl_3$ have % $T_{\lambda 400-700}$ greater than 80% with 7 mol% displaying the highest visible light transmission of 85%. This suggests that Cl-doping is an effective method to increase the optical transparency of ZnO thin films while electrical conductivity is preserved, this has also been described previously.[26,30–33] It is interesting to note that attempts to use $ZnCl_2$ in place of $FeCl_3$ to form Cl-doped ZnO films resulted in the formation of grey, hazy and poorly adhered films with very low Cl incorporation.

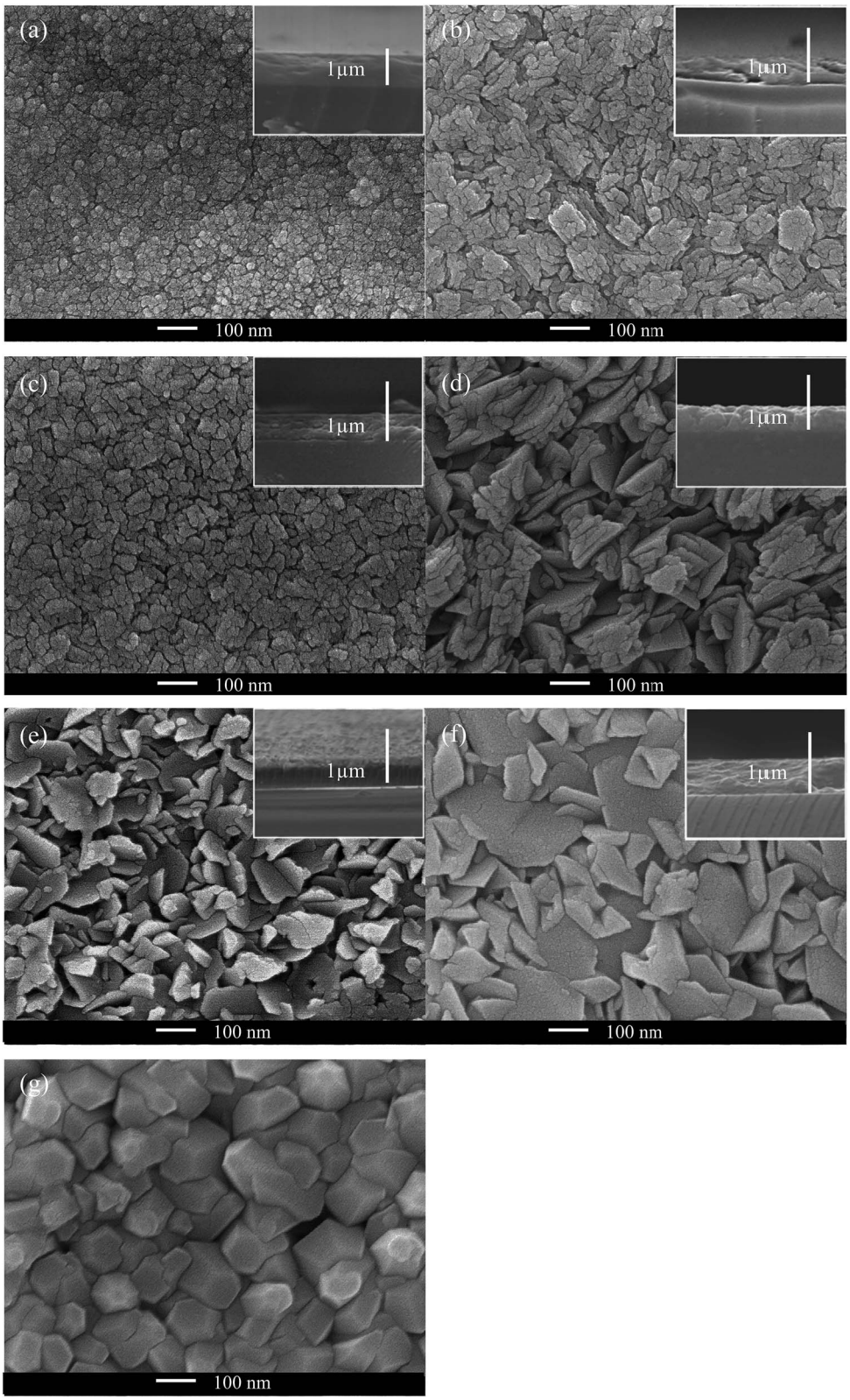

Fig. 6 SEM images of ZnO and Cl-doped ZnO films with mol% $FeCl_3$ loading of (a) 0 mol%, (b) 1 mol%, (c) 3 mol%, (d) 5 mol%, (e) 7 mol%, (f) 10 mol% and (g) 15 mol%. Side-on SEM (inset) shows film thickness.

To obtain the band gap energy, the optical properties of the films have been measured. The Tauc plot (Fig. 10), which is the plot of $(\alpha h\nu)^2$ *vs.* $h\nu$ was utilised to estimate the band gap energy for ZnO. The absorption coefficient (α) was obtained from Lambert's equation: $\alpha = 1/t[2 - \log(\%\ T)]$ where t and % T are the film thickness and % transmittance, respectively. The band

Table 1 Cell parameters *a*, *c*, cell volume *V*, crystallite size and film thickness

Mol% $FeCl_3$	*a* (Å)	*c* (Å)	*V* (Å^3)	Crystallite size (Å)	Thickness (nm)
0	3.2506(11)	5.2067(11)	47.65(3)	207.23 ± 0.25	930
1	3.2505(7)	5.2091(12)	47.67(3)	297.07 ± 0.50	470
3	3.2511(4)	5.2089(8)	47.68(1)	276.80 ± 3.82	450
5	3.2523(2)	5.2119(5)	47.74(1)	328.83 ± 2.94	460
7	3.2536(4)	5.2134(5)	47.80(1)	406.97 ± 7.71	570
10	3.2539(4)	5.2152(4)	47.82(1)	377.27 ± 1.31	580
15	3.2553(2)	5.2133(1)	47.84(1)	518.97 ± 4.14	—

gap energy of ZnO was 3.31 ± 0.01 eV, which agrees with other works.[32,78–81] In the case of Cl-doped ZnO films, which are degenerated semiconducting films, the band gap was estimated from the corrected Tauc plot to amend the underestimation when the Tauc method is used.[82] The band gap of Cl-doped ZnO films increases from that of undoped films (Table 2). Previously DFT calculations have shown for Cl-doped ZnO that the substitution of O by Cl introduces a shallow donor state derived mainly from Cl 3s states. The Fermi level shifts to the CB, resulting in an increase in optical band gap energy according to the Burstein–Moss effect.[83] However, the variation in Cl content does not significantly affect the band gap energy.

Electrical properties. Hall effect data was obtained for the samples, as shown in Table 2. The resistivity of the undoped ZnO films prepared in this work (1.4×10^{-1} Ω cm) were similar to that reported previously (1.3×10^{-1} Ω cm) for films deposited using Zn acetate dihydrate in methanol *via* AACVD.[82]

It can be seen that on substitution of Cl in ZnO films a lower resistivity was obtained from that of undoped ZnO film, which can be rationalised from the donor electrons generated from Cl. As mentioned earlier, the DFT calculation shows that the substitution of O by Cl introduces a shallow donor state derived mainly from Cl 3s states. The Fermi level shifts to the CB, thus results in n-type semiconducting behavior.[83] This is also

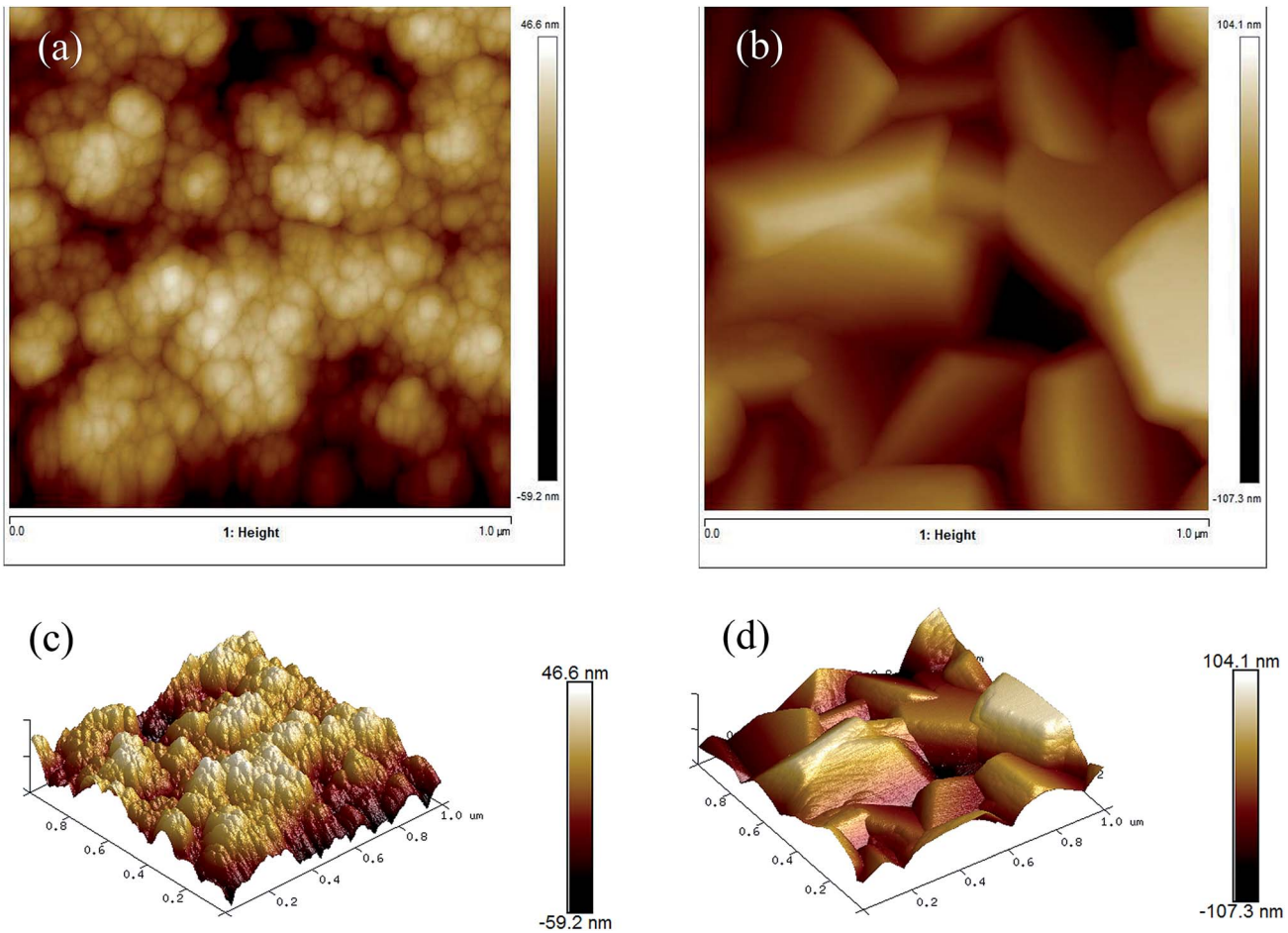

Fig. 7 AFM images of (a) undoped ZnO and (b) 10 mol% $FeCl_3$ doped ZnO and 3D images of the same area (c) and (d).

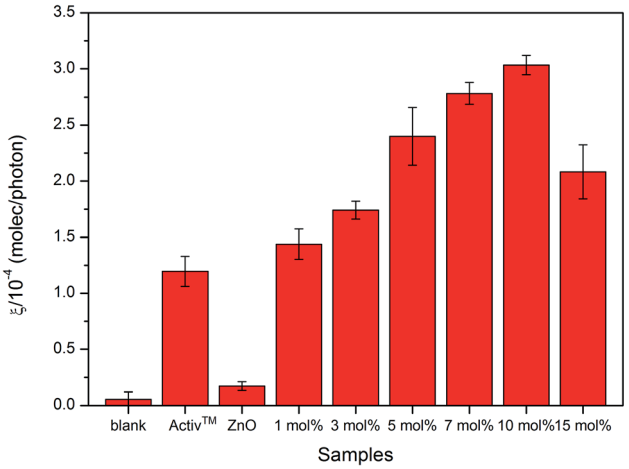

Fig. 8 The formal quantum efficiency (FQE) for the degradation of stearic acid on undoped and Cl-doped ZnO films under UVA illumination. Pilkington Activ glass is used as reference. All ZnO:Cl films are photocatalytically active and 10 mol% $FeCl_3$ added show the best efficiency.

confirmed with negative value of carrier concentration. The film from 5 mol% $FeCl_3$ exhibited the lowest electrical resistivity of $4.28 \pm 0.41 \times 10^{-2}$ Ω cm, the carrier concentration of $1.76 \pm 0.13 \times 10^{19}$ cm^{-3} and the carrier mobility of 8.66 ± 1.47 $cm^2\ V^{-1}\ s^{-1}$.

The Cl-doped ZnO films prepared in this work have electrical resistivity in the same order of magnitude comparing to those obtained using atomic layer deposition (0.55 at% Cl-doped ZnO films: $\rho = 1.215 \times 10^{-2}$ Ω cm, $n = 5.901 \times 10^{19}$ cm^{-3} and $\mu = 31.81$ $cm^2\ V^{-1}\ s^{-1}$)[32] and metal–organic CVD ($\rho = 3.6 \times 10^{-2}$ Ω cm, $n \sim 10^{20}$ cm^{-3} and $\mu = 9$–14 $cm^2\ V^{-1}\ s^{-1}$),[31,34] but higher than that prepared by physical layer deposition (2.4 at% Cl-doped ZnO films: $\rho = 6.344 \times 10^{-4}$ Ω cm, $n = 4.04 \times 10^{20}$ cm^{-3} and $\mu = 23.75$ $cm^2\ V^{-1}\ s^{-1}$).[30,33] Computational studies

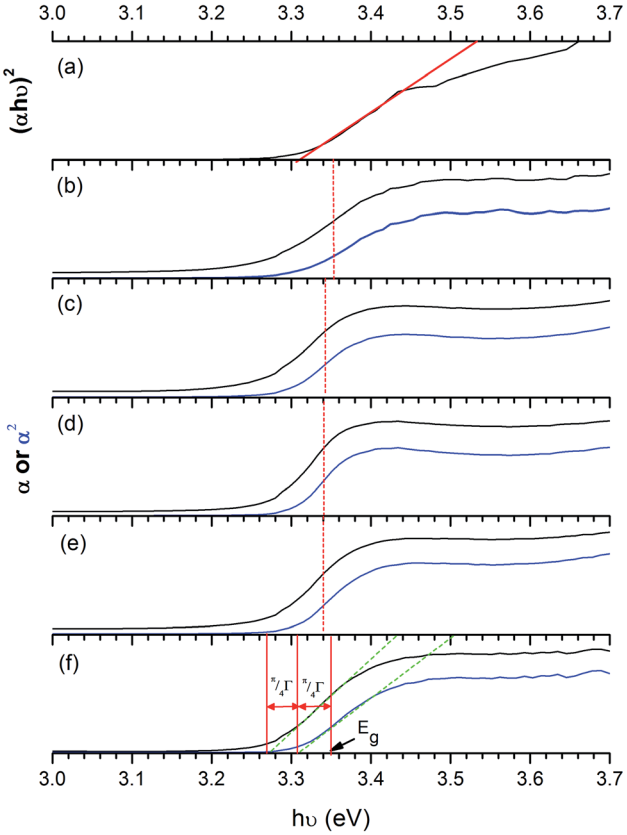

Fig. 10 Tauc plots of ZnO films (a) and the corrected Tauc plot of ZnO:Cl films with 1 mol% (b), 3 mol% (c), 5 mol% (d), 7 mol% (e) and 10 mol% Cl (f). A broadening parameter $\pi/4\Gamma$ is obtained from the separation of extrapolations along the edge of α (black) and α^2 (blue) plots against $h\nu$, then the parameter is added to the uncorrected band gap to obtain a corrected estimate, as discussed by Poeppelmeier *et al.*[84] The extrapolated lines on x-axis show band gap energy (E_g). The band gap energy obtained from ZnO:Cl films is larger than that of undoped ZnO films according to Burstein–Moss effect.

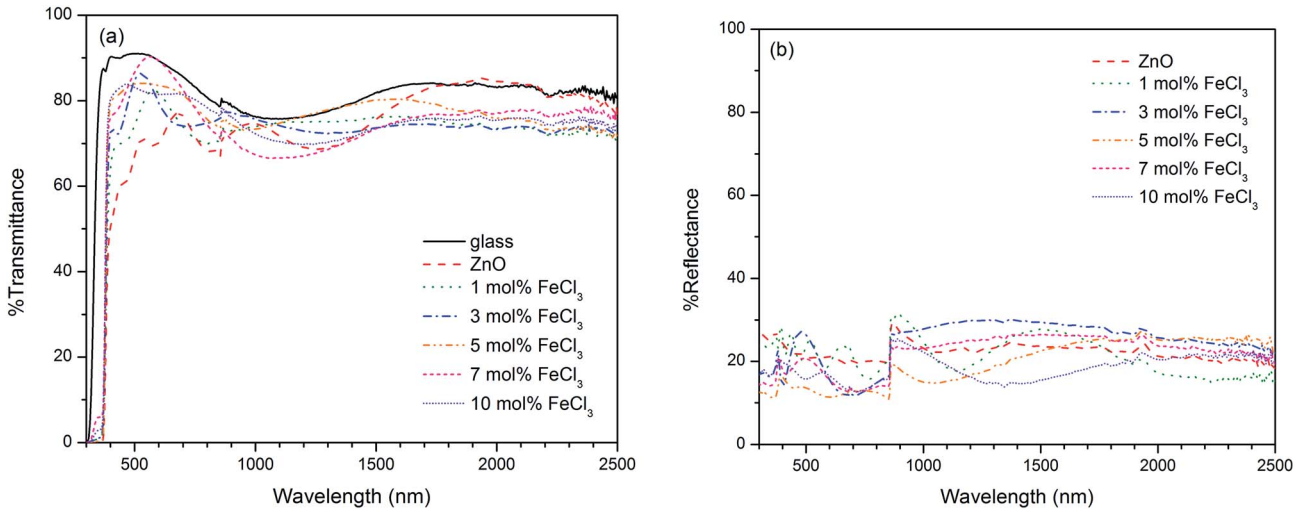

Fig. 9 (a) Transmittance and (b) reflectance spectra of all films and the spectrum of bare glass was collected as reference. ZnO:Cl films improve % T from carbon-contaminated undoped ZnO film. The films with 7 mol% $FeCl_3$ exhibits the highest % T of 85.

Table 2 Functional properties: photocatalytic properties and TCO properties, which includes electrical properties and optical properties[a]

	Photocatalytic properties	TCO properties					
		Optical properties		Electrical properties			
Mol% $FeCl_3$	ξ ($\times 10^{-4}$ molecule per photon)	% $T_{\lambda 400-700}$	E_g (eV)	n ($\times 10^{19}$ cm^{-3})	μ (cm^2 V^{-1} s^{-1})	ρ ($\times 10^{-2}$ Ω cm)	R_{sh} (Ω □$^{-1}$)
0	0.17 ± 0.04	68	3.31 ± 0.01	0.10 ± 0.01	4.34 ± 0.12	1400.00 ± 44.97	15 053.8 ± 483.6
1	1.44 ± 0.14	76	3.35 ± 0.01	0.86 ± 0.11	6.35 ± 0.84	11.91 ± 0.01	2532.9 ± 0.8
3	1.74 ± 0.08	79	3.34 ± 0.01	0.97 ± 0.23	11.79 ± 1.38	5.99 ± 0.75	1331.9 ± 167.4
5	2.40 ± 0.26	83	3.34 ± 0.01	1.76 ± 0.13	8.66 ± 1.47	4.28 ± 0.41	929.8 ± 89.46
7	2.78 ± 0.10	85	3.34 ± 0.01	1.11 ± 0.30	9.90 ± 1.04	6.41 ± 1.13	1124.6 ± 198.8
10	3.03 ± 0.09	82	3.35 ± 0.01	3.24 ± 1.13	4.00 ± 1.22	6.18 ± 0.33	1064.8 ± 57.2
15	2.08 ± 0.24	—	—	—	—	—	—

[a] n: charge carrier concentration; μ: charge carrier mobility; ρ: bulk resistivity; R_{sh}: sheet resistance; ξ: formal quantum yield efficiency.

have previously revealed that oxygen vacancy is the donor-type defect which show the lowest formation energy under n-type conditions; therefore it may also be valuable to take oxygen deficiency into an account for the conductivity in ZnO film prepared under an inert atmosphere like N_2.[85] It is also interesting to mention that the thermodynamic study using Kröger method proposed the possible defect impurities in Cl-doped ZnO, which are Zn vacancy (V_{Zn}), Zn interstitial (Z_i), oxygen vacancy (V_O) and chlorine donor (Cl_O).[86] The defect in ZnO system is well known to be strongly correlated to preparation condition including temperature and atmosphere. This suggests that the film deposition route is an important factor affecting the electrical properties of synthesised films.

These results show that deposition of electrically conductive and transparent Cl-doped ZnO films onto inexpensive glass substrates can be achieved *via* a one-step AACVD method without the requirement for post-deposition annealing or expensive vacuum apparatus. We have shown that the properties of the resulting Cl-doped ZnO thin films can be tailored to a specific application *via* altering the electronic, crystal and surface texture properties of the films. Thus, the Cl-doped ZnO films deposited *via* this simple AACVD route combine three functional properties (optical transparency, electrical conductivity and photocatalysis) within the same film making it a promising alternative to conventional TCO or photocatalytic materials. Furthermore, AACVD technique shows the potential to provide multifunctional properties by tuning some parameters, *e.g.*, morphology, preferred orientation and surface roughness.

Conclusions

Cl-doped ZnO films have been successfully prepared *via* aerosol-assisted CVD for the first time from Zn acetate dihydrate and $FeCl_3$ in methanol. The substitution of Cl at O site into the ZnO lattice was confirmed by the obtained pure phase of wurtzite ZnO for all films and the increase in cell parameters *a*, *c* and cell volume, as well as the presence of Cl 1s XPS spectra. Fe was not found in the films, which might be due to side reactions of Fe compounds as some red precipitates were observed in the bubbler after deposition. The Cl-doping significantly affected the morphology of the synthesised thin films. TCO properties were achieved from Cl substitution as high transmittance above 80% and low electrical resistivity in the order of 10^{-2} Ω cm were observed. The highest transmittance (% *T*) of 85% was obtained when using 7 mol% $FeCl_3$ in the precursor and the lowest resistivity of $4.28 \pm 0.41 \times 10^{-2}$ Ω cm was obtained for 5 mol% $FeCl_3$. In contrast, the use of 10 mol% $FeCl_3$ doping resulted in Cl-doped ZnO thin films which exhibited the best photocatalytic activity of stearic acid degradation under UVA irradiation with the highest formal quantum efficiency (FQE) of $3.0 \pm 0.1 \times 10^{-4}$ molecule per photon. AFM images implied that the improvement in photocatalytic activity results from surface morphology and exposed crystal faces since the specific surface area of Cl-doped ZnO films from 10 mol% $FeCl_3$ were not significantly different from that of plain ZnO films. The surface morphology, optoelectronic properties and crystallinity have been shown to be dependent on the amount of $FeCl_3$ present in the precursor solution. These films showed potential application as both TCOs and photocatalysts; these multifunctional characteristics expand the scope of applications such as self-cleaning[87–89] flat panel displays. Furthermore, the AACVD methodology could be utilised to tailor the functional properties of the films towards specific applications, such as for photocatalytic materials or TCOs for photovoltaic devices.

Conflicts of interest

There are no conflicts to declare.

Acknowledgements

The Development and Promotion of Science and Technology Talents Project (DPST) is acknowledged for the study of A. Jiamprasertboon. MJP and CJC would like to thank the EPSRC for grant EP/L017709. YL acknowledges the support from EPSRC project EP/N024915/1. The authors would like to thank NSG Pilkington Glass Ltd. Sapna D. Ponja is acknowledged for Le Bail refinement guidance and Premrudee Promdet is acknowledged for mass spectrometry experiment.

References

1 R. G. Gordon, *MRS Bull.*, 2000, **25**, 52–57.
2 D. S. Ginley and J. D. Perkins, in *Handbook of transparent conductors*, 2011, pp. 1–25.
3 S. C. Dixon, D. O. Scanlon, C. J. Carmalt and I. P. Parkin, *J. Mater. Chem. C*, 2016, **4**, 6946–6961.
4 C. G. Granqvist and A. Hultåker, *Thin Solid Films*, 2002, **411**, 1–5.
5 D. S. Bhachu, M. R. Waugh, K. Zeissler, W. R. Branford and I. P. Parkin, *Chem.–Eur. J.*, 2011, **17**, 11613–11621.
6 C.-C. Lin, M.-C. Chiang and Y.-W. Chen, *Thin Solid Films*, 2009, **518**, 1241–1244.
7 U.S. Department of the Interior and U.S. Geological Survey, *Mineral commodity summaries 2017*, U.S. Geological Survey, 2017, vol. 1.
8 J. Hu and R. G. Gordon, *J. Appl. Phys.*, 1992, **71**, 880–890.
9 S. K. Ghandhi, R. J. Field and J. R. Shealy, *Appl. Phys. Lett.*, 1980, **37**, 449–451.
10 N. Hollingsworth, A. L. Johnson, A. Kingsley, G. Kociok-Köhn and K. C. Molloy, *Organometallics*, 2010, **29**, 3318–3326.
11 C. S. McNally, D. P. Turner, A. N. Kulak, F. C. Meldrum and G. Hyett, *Chem. Commun.*, 2012, **48**, 1490–1492.
12 M. R. Waugh, G. Hyett and I. P. Parkin, *Chem. Vap. Depos.*, 2008, **14**, 369–372.
13 J. A. Manzi, C. E. Knapp, I. P. Parkin and C. J. Carmalt, *Thin Solid Films*, 2016, **616**, 477–481.
14 S. Kuprenaite, T. Murauskas, A. Abrutis, V. Kubilius, Z. Saltyte and V. Plausinaitiene, *Surf. Coating. Technol.*, 2015, **271**, 156–164.
15 D. B. Potter, D. S. Bhachu, M. J. Powell, J. A. Darr, I. P. Parkin and C. J. Carmalt, *Phys. Status Solidi A*, 2016, **213**, 1346–1352.
16 S. D. Ponja, S. Sathasivam, I. P. Parkin and C. J. Carmalt, *RSC Adv.*, 2014, **4**, 49723–49728.
17 D. B. Potter, M. J. Powell, I. P. Parkin and C. J. Carmalt, *J. Mater. Chem. C*, 2018, **6**, 588–597.
18 D. P. Howard, P. Marchand, L. McCafferty, C. J. Carmalt, I. P. Parkin and J. A. Darr, *ACS Comb. Sci.*, 2017, **19**, 239–245.
19 D. P. Howard, P. Marchand, I. D. Johnson, C. J. Carmalt, I. P. Parkin and J. A. Darr, *J. Mater. Chem. A*, 2016, **4**, 12774–12780.
20 S. C. Dixon, S. Sathasivam, B. A. D. Williamson, D. O. Scanlon, C. J. Carmalt and I. P. Parkin, *J. Mater. Chem. C*, 2017, **5**, 7585–7597.
21 D. B. Potter, M. J. Powell, J. A. Darr, I. P. Parkin and C. J. Carmalt, *RSC Adv.*, 2017, **7**, 10806–10814.
22 D. P. Howard, P. Marchand, C. J. Carmalt, I. P. Parkin and J. A. Darr, *J. Mater. Chem. C*, 2017, **5**, 8796–8801.
23 G. Walters and I. P. Parkin, *Appl. Surf. Sci.*, 2009, **255**, 6555–6560.
24 H. M. Yates, J. M. Gaskell, M. E. Thomson, D. W. Sheel, B. Delaup and M. Morales-Masis, *Thin Solid Films*, 2015, **590**, 260–265.
25 H. Y. Xu, Y. C. Liu, R. Mu, C. L. Shao, Y. M. Lu, D. Z. Shen and X. W. Fan, *Appl. Phys. Lett.*, 2005, **86**, 1–3.
26 J. Rousset, E. Saucedo and D. Lincot, *Chem. Mater.*, 2009, **21**, 534–540.
27 X. Yang, A. Wolcott, G. Wang, A. Sobo, R. C. Fitzmorris, F. Qian, J. Z. Zhang and Y. Li, *Nano Lett.*, 2009, **9**, 2331–2336.
28 S. Mohri, Y. Hirose, S. Nakao, N. Yamada, T. Shimada and T. Hasegawa, *J. Appl. Phys.*, 2012, **111**, 93528.
29 J. Hu and R. G. Gordon, *Sol. Cell.*, 1991, **30**, 437–450.
30 J. C. Lee, N. G. Subramaniam, J. W. Lee, J. C. Lee and T. W. Kang, *Phys. Status Solidi A*, 2013, **210**, 2638–2643.
31 E. Chikoidze, M. Nolan, M. Modreanu, V. Sallet and P. Galtier, *Thin Solid Films*, 2008, **516**, 8146–8149.
32 Y.-J. Choi, K.-M. Kang, H.-S. Lee and H.-H. Park, *J. Mater. Chem. C*, 2015, **3**, 8336–8343.
33 J. Lee, E. Park, N. G. Subramaniam, J. Lee, J. Lee, J. Lee and T. Kang, *Curr. Appl. Phys.*, 2012, **12**, S80–S84.
34 E. Chikoidze, M. Modreanu, V. Sallet, O. Gorochov and P. Galtier, *Phys. Status Solidi A*, 2008, **205**, 1575–1579.
35 J. Rousset, E. Saucedo, K. Herz and D. Lincot, *Prog. Photovoltaics Res. Appl.*, 2011, **19**, 537–546.
36 P. Marchand, I. A. Hassan, I. P. Parkin and C. J. Carmalt, *Dalton Trans.*, 2013, **42**, 9406.
37 M. J. Powell and C. J. Carmalt, *Chem.–Eur. J.*, 2017, **23**, 15543–15552.
38 X.-T. Yan and Y. Xu, in *An Integrated Engineering Design for Advanced Materials*, 2010, p. 356.
39 A. Kafizas, N. Noor, P. Carmichael, D. O. Scanlon, C. J. Carmalt and I. P. Parkin, *Adv. Funct. Mater.*, 2014, **24**, 1758–1771.
40 S. Sathasivam, D. S. Bhachu, Y. Lu, N. Chadwick, S. A. Althabaiti, A. O. Alyoubi, S. N. Basahel, C. J. Carmalt and I. P. Parkin, *Sci. Rep.*, 2015, **5**, 10952.
41 D. S. Bhachu, S. Sathasivam, G. Sankar, D. O. Scanlon, G. Cibin, C. J. Carmalt, I. P. Parkin, G. W. Watson, S. M. Bawaked, A. Y. Obaid, S. Al-Thabaiti and S. N. Basahel, *Adv. Funct. Mater.*, 2014, **24**, 5075–5085.
42 C. Sotelo-Vazquez, N. Noor, A. Kafizas, R. Quesada-Cabrera, D. O. Scanlon, A. Taylor, J. R. Durrant and I. P. Parkin, *Chem. Mater.*, 2015, **27**, 3234–3242.
43 a C. Larson and R. B. Von Dreele, *Structure*, 2004, **748**, 86–748.
44 B. H. Toby, *J. Appl. Crystallogr.*, 2001, **34**, 210–213.
45 A. Mills and J. Wang, *J. Photochem. Photobiol. Chem.*, 2006, **182**, 181–186.
46 A. J. Chen, X. M. Wu, Z. D. Sha, L. J. Zhuge and Y. D. Meng, *J. Phys. D: Appl. Phys.*, 2006, **39**, 4762–4765.
47 S. Saha, M. Tomar and V. Gupta, *J. Appl. Phys.*, 2012, **111**, 102804.
48 B. P. Kafle, S. Acharya, S. Thapa and S. Poudel, *Ceram. Int.*, 2016, **42**, 1133–1139.
49 K. Singh, V. Devi, R. Dhar and D. Mohan, *Superlattices Microstruct.*, 2015, **85**, 433–437.
50 P. Ariyakkani, L. Suganya and B. Sundaresan, *J. Alloys Compd.*, 2017, **695**, 3467–3475.
51 A. Gorzkowska-Sobas, A. Galeckas, M. F. Sunding, S. Diplas and A. Y. Kuznetsov, *Phys. Scr.*, 2010, **T141**, 14004.
52 V. S. Santhosh, K. Rajendra Babu and M. Deepa, *J. Mater. Sci.: Mater. Electron.*, 2014, **25**, 224–232.

53 A. K. Yadav, S. M. Haque, S. Tripathi, D. Shukla, M. A. Ahmed, D. M. Phase, S. Bandyopadhyay, S. N. Jha and D. Bhattacharyya, *RSC Adv.*, 2016, **6**, 74982–74990.
54 A. P. Rambu, V. Nica and M. Dobromir, *Superlattices Microstruct.*, 2013, **59**, 87–96.
55 R. C. Paul, R. C. Narula and S. K. Vasisht, *Transit. Met. Chem.*, 1978, **3**, 35–38.
56 A. Laurikenas, J. Barkauskas, J. Reklaitis, G. Niaura, D. Baltrunas and A. Kareiva, *Lithuanian J. Phys.*, 2016, **56**, 35–41.
57 L. G. Mar, P. Y. Timbrell and R. N. Lamb, *Thin Solid Films*, 1993, **223**, 341–347.
58 G. Deroubaix and P. Marcus, *Surf. Interface Anal.*, 1992, **18**, 39–46.
59 M. Chen, X. Wang, Y. H. Yu, Z. L. Pei, X. D. Bai, C. Sun, R. F. Huang and L. S. Wen, *Appl. Surf. Sci.*, 2000, **158**, 134–140.
60 J.-W. Park, H. S. So, H.-M. Lee, H.-J. Kim, H.-K. Kim and H. Lee, *J. Appl. Phys.*, 2015, **117**, 155305.
61 M. N. Islam, T. B. Ghosh, K. L. Chopra and H. N. Acharya, *Thin Solid Films*, 1996, **280**, 20–25.
62 H. Xue, Y. Chen, X. L. Xu, G. H. Zhang, H. Zhang and S. Y. Ma, *Phys. E*, 2009, **41**, 788–791.
63 R. Simpson, R. G. White, J. F. Watts and M. A. Baker, *Appl. Surf. Sci.*, 2017, **405**, 79–87.
64 M. A. Baker, R. Gilmore, C. Lenardi and W. Gissler, *Appl. Surf. Sci.*, 1999, **150**, 255–262.
65 D. Bao, H. Gu and A. Kuang, *Thin Solid Films*, 1998, **312**, 37–39.
66 S.-H. Ko Park and Y. E. Lee, *J. Mater. Sci.*, 2004, **39**, 2195–2197.
67 Z. Tao, X. Yu, X. Fei, J. Liu, G. Yang, Y. Zhao, S. Yang and L. Yang, *Opt. Mater.*, 2008, **31**, 1–5.
68 R. Yousefi and F. Jamali-Sheini, *Ceram. Int.*, 2012, **38**, 5821–5825.
69 R. Yousefi, A. K. Zak and M. R. Mahmoudian, *J. Solid State Chem.*, 2011, **184**, 2678–2682.
70 J. Fan, A. Shavel, R. Zamani, C. Fábrega, J. Rousset, S. Haller, F. Güell, A. Carrete, T. Andreu, J. Arbiol, J. R. Morante and A. Cabot, *Acta Mater.*, 2011, **59**, 6790–6800.
71 R. D. Shannon, *Acta Crystallogr., Sect. A: Cryst. Phys., Diffr., Theor. Gen. Crystallogr.*, 1976, **32**, 751–767.
72 S. Chen, R. M. Wilson and R. Binions, *J. Mater. Chem. A*, 2015, **3**, 5794–5797.
73 R. Quesada-Cabrera, C. Sotelo-Vazquez, J. A. Darr and I. P. Parkin, *Appl. Catal., B*, 2014, **160–161**, 582–588.
74 W. Wang, T. Ai and Q. Yu, *Sci. Rep.*, 2017, **7**, 42615.
75 S.-Y. Pung, W.-P. Lee and A. Aziz, *Int. J. Inorg. Chem.*, 2012, **2012**, 1–9.
76 C. Yu, F. Cao, X. Li, G. Li, Y. Xie, J. C. Yu, Q. Shu, Q. Fan and J. Chen, *Chem. Eng. J.*, 2013, **219**, 86–95.
77 G. Byzynski, C. Melo, D. P. Volanti, M. M. Ferrer, A. F. Gouveia, C. Ribeiro, J. Andrés and E. Longo, *Mater. Des.*, 2017, **120**, 363–375.
78 D. G. Thomas, *J. Phys. Chem. Solids*, 1960, **15**, 86–96.
79 R. L. Hengehold, R. J. Almassy and F. L. Pedrotti, *Phys. Rev. B*, 1970, **1**, 4784–4791.
80 W. Y. Liang and A. D. Yoffe, *Phys. Rev. Lett.*, 1968, **20**, 59–62.
81 T. K. Gupta, *J. Am. Ceram. Soc.*, 1990, **73**, 1817–1840.
82 S. C. Dixon, S. Sathasivam, B. A. D. Williamson, D. O. Scanlon, C. J. Carmalt and I. P. Parkin, *J. Mater. Chem. C*, 2017, **5**, 7585–7597.
83 A. Slassi, *Optik*, 2015, **126**, 4751–4756.
84 A. Dolgonos, T. O. Mason and K. R. Poeppelmeier, *J. Solid State Chem.*, 2016, **240**, 43–48.
85 F. Oba, S. R. Nishitani, S. Isotani, H. Adachi and I. Tanaka, *J. Appl. Phys.*, 2001, **90**, 824–828.
86 T. Tchelidze, E. Chikoidze, O. Gorochov and P. Galtier, *Thin Solid Films*, 2007, **515**, 8744–8747.
87 S. Afzal, W. A. Daoud and S. J. Langford, *J. Mater. Chem. A*, 2014, **2**, 18005–18011.
88 I. P. Parkin and R. G. Palgrave, *J. Mater. Chem.*, 2005, **15**, 1689–1695.
89 S. Banerjee, D. D. Dionysiou and S. C. Pillai, *Appl. Catal., B*, 2015, **176–177**, 396–428.